Brain Stimulation 13 (2020) 412–419

Contents lists available at ScienceDirect

Brain Stimulation

journal homepage: http://www.journals.elsevier.com/brain-stimulation

High density microelectrode recording predicts span of therapeutic tissue activation volumes in subthalamic deep brain stimulation for Parkinson disease

Charles W. Lu [a, b], Karlo A. Malaga [a, b], Kelvin L. Chou [b, c], Cynthia A. Chestek [a], Parag G. Patil [a, b, c, *]

[a] University of Michigan, Department of Biomedical Engineering, Carl A. Gerstacker Building, 2200 Bonisteel Blvd, Ann Arbor, MI, 48109, USA
[b] University of Michigan, Department of Neurosurgery, 1500 E Medical Center Drive, Ann Arbor, MI, 48109, USA
[c] University of Michigan, Department of Neurology, 1500 E Medical Center Drive, Ann Arbor, MI, 48109, USA

ARTICLE INFO

Article history:
Received 14 December 2018
Received in revised form
26 November 2019
Accepted 27 November 2019
Available online 4 December 2019

Keywords:
Parkinson disease
Deep brain stimulation
Subthalamic nucleus
Microelectrode recording
Tissue activation volumes

ABSTRACT

Background: Subthalamic deep brain stimulation alleviates motor symptoms of Parkinson disease by activating precise volumes of neural tissue. While electrophysiological and anatomical correlates of clinically effective electrode sites have been described, therapeutic stimulation likely acts through multiple distinct neural populations, necessitating characterization of the full span of tissue activation. Microelectrode recordings have yet to be mapped to therapeutic tissue activation volumes and surveyed for predictive markers.

Objective: Combine high-density, broadband microelectrode recordings with detailed computational models of tissue activation to describe and to predict regions of therapeutic tissue activation.

Methods: Electrophysiological features were extracted from microelectrode recordings along 23 subthalamic deep brain stimulation implants in 16 Parkinson disease patients. These features were mapped in space against tissue activation volumes of therapeutic stimulation, modeled using clinically-determined stimulation programming parameters and fully individualized, atlas-independent anisotropic tissue properties derived from 3T diffusion tensor magnetic resonance images. Logistic LASSO was applied to a training set of 17 implants out of the 23 implants to identify predictors of therapeutic stimulation sites in the microelectrode recording. A support vector machine using these predictors was used to predict therapeutic activation. Performance was validated with a test set of six implants.

Results: Analysis revealed wide variations in the distribution of therapeutic tissue activation across the microelectrode recording-defined subthalamic nucleus. Logistic LASSO applied to the training set identified six oscillatory predictors of therapeutic tissue activation: theta, alpha, beta, high gamma, high frequency oscillations (HFO, 200–400 Hz), and high frequency band (HFB, 500–2000 Hz), in addition to interaction terms: theta x HFB, alpha x beta, beta x HFB, and high gamma x HFO. A support vector classifier using these features predicted therapeutic sites of activation with 64% sensitivity and 82% specificity in the test set, outperforming a beta-only classifier. A probabilistic predictor achieved 0.87 area under the receiver-operator curve with test data.

Conclusions: Together, these results demonstrate the importance of personalized targeting and validate a set of microelectrode recording signatures to predict therapeutic activation volumes. These features may be used to improve the efficiency of deep brain stimulation programming and highlight specific neural oscillations of physiological importance.

Introduction

Deep brain stimulation of the subthalamic nucleus (STN DBS) is a well-established surgical treatment for Parkinson disease. Efficacious therapy requires both accurate surgical placement of DBS

Abbreviations: DBS, deep brain stimulation; STN, subthalamic nucleus; VTA, volume of tissue activation; HFO, high-frequency oscillations; HFB, high-frequency band; SVM, support vector machine.

* Corresponding author. Department of Neurosurgery, 1500 E Medical Center Drive, SPC 5338, Ann Arbor, MI, 48109-5338, USA.
E-mail address: pgpatil@med.umich.edu (P.G. Patil).

https://doi.org/10.1016/j.brs.2019.11.013

leads and careful programming of stimulation parameters. Together, these procedures ensure modulation of the correct neural pathways to achieve maximal therapeutic effect. However, conventional DBS programming to achieve optimal tissue activation is a time-consuming empirical process [1,2].

There exist both anatomical and electrophysiological approaches to prospectively identify therapeutic activation regions. Clinical observations [3–5] and computational models [6–8] both point to dorsal STN as an effective stimulation target. This region is traversed by the hyperdirect pathway [9], which has been strongly implicated in the therapeutic mechanisms of DBS [10,11]. Tissue activation models, in particular, have made notable contributions to this area of study. Although *in vivo* measurement of tissue activation is typically impractical, tissue activation models offer a sophisticated estimate of the anatomical region activated by therapeutic stimulation [12,13] and have strengthened hypotheses identifying dorsal STN and the hyperdirect pathway as optimal sites of stimulation [6,8]. Regions of elevated beta power observed on microelectrode recording have also been associated with effective DBS [14–21] and are often coincident with dorsal STN [17,22,23].

However, a growing body of evidence suggests that this is not the complete story. While the "average" active contact is often located near the dorsal STN border, maximally effective stimulation sites are known to vary significantly across patients [24,25]. This highlights a need to more precisely characterize the three-dimensional span of tissue activated by therapeutic stimulation, which has historically been analyzed as a solitary point [15,16,18,19]. Likewise, a number of subthalamic oscillations outside the beta band—notably alpha, gamma, and high frequency oscillations—are known to play key roles in Parkinsonian neurophysiology [25–32] and potentially interact in clinically meaningful ways, such as phase-amplitude coupling [25,28,31,33]. These observations suggest a need to more holistically interpret the anatomical and electrophysiological loci of STN DBS intervention to better understand optimal physiological sites of action.

Here, we analyze fully individualized anisotropic models of therapeutic tissue activation alongside high-density, broadband electrophysiology. We bring together these complementary modes of study into a unified analysis of therapeutic stimulation, by mapping microelectrode recordings to clinically-derived tissue activation models. By incorporating individual heterogeneous anisotropy into our models, we achieve precise patient-specific estimates of tissue activation [34,35]. We describe a data-driven approach to identify associations between regions of therapeutic tissue activation and broadband electrophysiological features, including cross-frequency interactions. We then show that selected signal features can be used to accurately predict spans of therapeutic activation in a test set of data.

Materials and methods

Patients

Subjects included 16 patients (11 men and 5 women) with advanced idiopathic Parkinson disease who underwent STN DBS surgery at the University of Michigan. Patient selection criteria for STN DBS at the institution have been described previously [36]. All patients were implanted bilaterally with Medtronic DBS leads, model 3389. Leads were placed with guidance by 3T magnetic resonance imaging (MRI), stereotactic navigation, and microelectrode recording. Subjects were STN DBS patients with stable programming parameters and subjectively satisfactory clinical outcomes 6 months after surgery. Subjects had a mean (standard deviation) age of 63 (6.1) years and mean disease duration of 10 (4.6) years. Stimulation amplitudes ranged from 1.7 to 4.8 (mean 2.8 V), with pulse width of 60 μs and frequencies of 125–185 Hz. Three implanted leads utilized two adjacent active contacts; all others utilized one active contact. Average DBS OFF and DBS ON MDS-UPDRS part III scores off medication were 45 (19) and 31 (17), with 25% improvement due to STN DBS stimulation. The study was approved by the University of Michigan Institutional Review Board, and all participants provided individual informed consent.

DBS lead placement

Patients underwent frame-based awake DBS surgery with microelectrode recording. Planned targets were initially assigned from indirect targeting (12 mm lateral, 3 mm posterior, and 4 mm inferior to the mid-commissural point), with adjustment from direct magnetic resonance visualization of the ventral border of STN, on 3T MRI (field of view = 200 mm × 200 mm, 0.69 x 0.69 × 1.25 mm voxels) (Philips Achieva 3T; Philips, Amsterdam, Netherlands). Recordings were performed from 15 mm above to 5 mm below the planned target on a single trajectory. Microelectrode signals were recorded at the tip of a bipolar microelectrode (MicroTargeting Electrode; FHC, Bowdin, ME), amplified (D360 Isolated Patient Amplifier System; Digitimer, Hertfordshire, England), and recorded to a computer using custom software (LabVIEW 2015; National Instruments, Austin, TX). An electrophysiologist identified the dorsal and ventral borders of the STN during surgery. DBS leads were then inserted with the tip near the ventral border of the electrophysiologically identified STN. Intraoperative confirmation of the microelectrode trajectory and DBS lead placement were performed using fluoroscopy. Additional details of the surgical procedure are described in previous publications [36,37].

Location of DBS electrode contacts

A high-resolution computed tomographic (CT) scan (GE HD750; General Electric, Boston, MA) was performed 2 to 4 weeks after surgery to visualize the location of DBS leads and individual electrode contacts. CT images were resampled via linear interpolation to match the resolution of the MRI images and oriented in Talairach space via coregistration to Talairach-oriented MR images using a mutual-information algorithm in commercial software (Analyze, AnalyzeDirect, Overland Park, KS). Additional detail can be found in [37]. Contacts were then directly visualized in 3D image reconstructions and coordinates were exported to MATLAB (MathWorks, Natick, MA) software for further analysis.

Tissue activation modeling

Preoperative diffusion tensor imaging (DTI) data for each patient were acquired using a single-shot echo planar imaging sequence with a dS-SENSE parallel-imaging scheme (reduction factor = 2, field of view = 224 mm × 224 mm, 1 x 1 × 2 mm voxels). Diffusion weighting was encoded along 16 independent orientations with a b-value of 800 s/mm^2. DTI images were resampled via cubic spline interpolation to match the resolution of the MRI images and oriented in Talairach space via coregistration to the Talairach-oriented MRI images in Analyze (Analyze 12.0; Mayo Clinic, Rochester, MN). The Analyze software DTI application was used to calculate the eigenvectors and eigenvalues of the DTI images. Diffusion tensors were then calculated from the eigenvectors and eigenvalues in MATLAB (MATLAB R2018b; MathWorks, Natick, MA) and converted to conductivity tensors using the linear relationship between conductivity and diffusion tensor eigenvalues ($\sigma/d \approx 0.844$ S s/mm^3) as described by Tuch et al. [38].

3D finite element models of therapeutic DBS were constructed for each patient in COMSOL (Multiphysics 5.2; COMSOL, Burlington, MA), incorporating each patient's entire MRI scan, the DBS lead, and clinically-determined stimulation parameters. Brain tissue was modeled as a block with DTI-derived anisotropic conductivity tensors linearly interpolated onto the adaptive mesh. The lead was modeled as an isotropically conductive Medtronic DBS lead, model 3389, (contact: 1.4×10^{7} S/m; insulation: 1×10^{-13} S/m) [39,40] positioned to match the coordinates of each patient's implanted DBS contacts, as measured from post-operative CT.

Boundary conditions were defined for the DBS electrode and bulk tissue. Specifically, an electric potential was applied to the surface of the active contact(s) according to programmed stimulation parameters of each patient, floating potentials were applied to the surfaces of the remaining contacts, and ground was applied to the surface of the brain tissue. Each patient's finite element model was meshed once individually, with finer meshing applied near the lead. Simulations were then run to solve for the electric potential in each model. The models were electrostatic, assuming frequency-independent gray matter impedance [41].

Tissue activation volumes (VTAs) were generated for each patient in COMSOL by calculating the spatial derivative of the electric potential [42,43] with activation thresholding at the level corresponding to each patient's clinical stimulation amplitude [44].

Microelectrode recording

Wideband (0.1 Hz −15 kHz) spiking activity and field potentials were recorded along the DBS probe trajectory at 0.5 mm intervals, spanning from 15 mm above to 5 mm below the surgical target (the STN ventral border on imaging), using the microelectrode recording tip. A typical trajectory traverses thalamus, fields of Forel, zona incerta, subthalamic nucleus, and substantia nigra. Seven seconds of uninterrupted electrophysiology was recorded at each site, with the first second of recording removed from analysis to eliminate movement artifact. Each trajectory had electrophysiology recorded at 30 to 48 sites. Microelectrode recordings less than 5 mm from the starting depth, which may have been affected by the cannula, were excluded from analysis. Recorded signal at each site was also visually examined for extraneous noise and excluded from analysis if found to be noisy. Data from 9 trajectories out of 32 implants were unavailable or excluded due to presence of significant noise. In total, microelectrode data from 641 sites were included in this analysis. Direct visualization of the microelectrode and the permanently implanted DBS lead using intraoperative fluoroscopy confirmed that both leads follow the same trajectory in the anteroposterior and dorsoventral directions. Post-operative migration of the DBS lead was assumed to be minimal. Using this relationship, electrophysiology was spatially mapped to each VTA model along the trajectory defined by the DBS lead visualized on post-operative CT.

At each depth, we calculated spike rate and the log of normalized power within the delta (0.1–4 Hz), theta (4–8 Hz), alpha (8–13 Hz), beta (13–30 Hz), low gamma (30–59 Hz), high gamma (61–200 Hz), high frequency oscillation (HFO; 200–400), and high frequency (HFB; 500–2000 Hz) bands [45]. In addition to main effects, first order interaction terms, calculated as the product of each pair of covariates, e.g., log(beta power) x log(low gamma power), were also considered during analysis. Spike rate was calculated by high pass filtering the microelectrode recording at 300 Hz and counting the number of threshold crossings at 4.5 times the signal's root mean square. For analysis of oscillations, spectra of each microelectrode recording were estimated using the fast Fourier transform. To remove 60 cycle noise, spectra values within 2.5 Hz of each 60 Hz harmonic was replaced with the median power within 5 Hz of the harmonic.

Classifier design and validation

Predictive electrophysiological parameters for forecasting of VTA spans were identified using logistic least absolute shrinkage and selection operator (logistic LASSO). LASSO is a well-established regression method that removes uninformative covariates from linear models, thereby selecting for features that provide predictive value [46]. This was carried out using MATLAB's built-in lassoglm() function. The function requires a regularization parameter, λ, which determines the penalization of non-zero slopes. A parameter sweep of λ was used to determine the optimal value of λ to minimize divergence observed in 300-fold cross validation. The final λ value used for parameter selection was one standard deviation greater than the optimal value to prevent overfitting, following the one standard error rule for model selection [47]. Parameterization of LASSO and covariate selection were performed using a training set of the data comprised of sites along 17 lead trajectories in 13 patients (out of a total of 23 implants in 16 patients), consisting of 486 sites.

The final classifier was a support vector machine (SVM) [48], used due to its robustness to extreme values which are often observed in electrophysiological data. The classifier incorporated the covariates identified by logistic LASSO, along with the first order terms implicated by selected interaction terms. The SVM was trained on the training data set using the MATLAB built-in fitcsvm() function, with a one standard deviation box constraint (to prevent overfitting to outliers) and assumption of uniform prior probabilities. (Since there are many more sites sampled outside of therapeutic VTAs than inside, an SVM trained on empirical prior probabilities will be biased toward classifying points as non-VTA.) Notably, the classifier analyzed each site *independently*, predicting whether it was inside or outside of the clinically-determined VTA, using electrophysiological features recorded at that site alone (Fig. 1A). The microelectrode recording from each site was analyzed independently of all other sites, without any spatial, trajectory, or subject information included in the analysis. Binary classifications from the SVM at each site were then spatially smoothed with a Gaussian window ($\sigma = 1$ mm) to produce a probabilistic prediction spanning the DBS lead trajectory (Fig. 1B). Performance of the smoothed prediction was characterized by a receiver-operator characteristic curve.

Performance of the SVM classifiers were determined using a holdout set of data comprised of electrophysiology from 155 sites (from six lead trajectories in three randomly selected patients not included in the training set). As such, classifier design and validation were achieved using wholly separate sets of data. This was done to ensure that classifier performance is not a result of overfitting to the training data.

The optimized SVM classifier was compared to both a beta-only classifier and a simple STN border-based approach to targeting and programing. The STN border approach assumes 2.8 V (cohort average) monopolar stimulation at the dorsal border of STN, identified in the microelectrode recording by an experienced clinical electrophysiologist. This passive approach to programming activates 2.0 mm of tissue in each direction along the span of the DBS lead (observed in two implants with 2.8 V monopolar stimulation).

Statistical analysis

All statistical tests were performed using MATLAB software. Statistical validation of classifier performance was determined

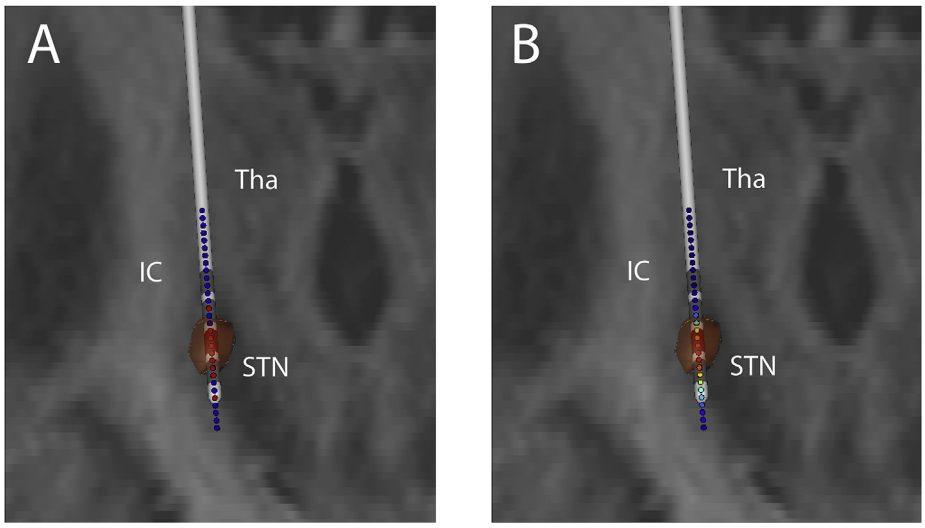

Fig. 1. Patient example of algorithm predictions projected upon the corresponding COMSOL model of clinically effective tissue activation and patient MRI. (A) SVM binary predictions of clinically activated sites. Sites predicted to be within the therapeutic VTA (shown in orange) are indicated with red circles; sites predicted to be outside indicated with blue. Active contact is shown in red. (B) The predictions shown in A are smoothed over space to produce a probabilistic prediction, accounting for the spatially contiguous nature of VTAs. Colors indicate probability of a site being within the therapeutic VTA, with hotter colors indicating higher probability. (For interpretation of the references to color in this figure legend, the reader is referred to the Web version of this article.)

using Fisher's exact test. Classifiers were compared using the McNemar test. Performance metrics are assessed using test data.

Results

Lead placement and tissue activation locations

DBS lead placement was found to vary across patients, with the average active contact located 1.9 mm ventral to the electrophysiological STN dorsal border. Tissue activation volumes modeled from clinically-determined stimulation parameters of different implants spanned regions above, within, and/or below the STN. 18% of observed VTA spans along the DBS lead were dorsal to STN, 37% within the dorsal half of STN, 36% within the ventral half of STN, and 9% ventral to STN.

Predictive electrophysiological features

A parameter sweep was used to determine the most appropriate regularization constant for logistic LASSO regression of VTA spans against microelectrode recordings. The sweep, performed using 300-fold cross-validation on the training set of 486 sites, yielded an optimal regularization constant of $\lambda = 0.00633$, with a standard deviation of 0.0308. Details of the parameter sweep are shown in Supplementary Figure 1. Re-running LASSO with a regularization constant equal to the optimal value plus the standard deviation ($\lambda = 0.0591$) identified five predictive neural features: HFB, theta x HFB, alpha x beta, beta x HFB, and high gamma x HFO. The main effects implicated by the interaction terms—theta, alpha, beta, high gamma, and HFO—were included as predictors for subsequent classifier analysis.

Support vector machine predictions

A support vector machine classifier was used to predict therapeutic tissue activation sites using ten electrophysiological features: theta, alpha, beta, high gamma, HFO, HFB, theta x HFB, alpha x beta, beta x HFB, and high gamma x HFO. The binary classifier achieved 77% accuracy, with 64% sensitivity and 82% specificity on the test set of 155 independently analyzed sites (Table 1). Performance was significantly above chance with an odds ratio of 8.4 (Fisher's exact test: $p < 10^{-6}$; 95% confidence interval: 3.8–18.5). Leave-one-out cross-validation (LOOCV) (partitioned by implant) of the support vector machine achieved similar overall performance. Binary predictions and VTA models for each trajectory analyzed in this study can be seen in Supplementary Figure 2. This model outperformed both a beta-only classifier (McNemar's test: $p < 10^{-6}$) and the STN border-based approach to targeting and programming (McNemar's test: $p = 0.1175$) (Table 1). Performance of the model was also evaluated against classifiers using individual frequency bands and a classifier using all available covariates (Supplementary Table 1). The model using LASSO-selected covariates achieved greater predictive value than all other classifiers. The HFB and spike rate-only classifiers were the highest-performing alternative models, both with accuracies of 74%.

While therapeutic activation sites may exist as isolated regions throughout the STN region, VTAs generated by conventional leads must be contiguous in space. To yield a more clinically useful prediction of VTA span reflecting this possibility, binary classifications of individually analyzed points were smoothed with a Gaussian window ($\sigma = 1$ mm) to be graded over space (Fig. 2). The smoothed predictions yielded probabilistic scores with an AUC of 0.87 for the test data (Fig. 3). Examination of individual trajectories in Fig. 2 reveals that classifier performance can vary by implant, with

Table 1
Classifier performance.

	Full model			Beta only		STN-border
	Train	Test	LOOCV	Train	Test	Test
Accuracy	0.76	0.77	0.73	0.51	0.52	0.70
Sensitivity	0.60	0.64	0.56	0.53	0.57	0.50
Specificity	0.85	0.82	0.83	0.50	0.50	0.77
PPV	0.67	0.57	0.63	0.35	0.30	0.45
NPV	0.81	0.86	0.91	0.67	0.76	0.81

Classifier performance using the full model determined by LASSO and using a beta-only model. PPV = positive predictive value; NPV = negative predictive value; LOOCV = leave-one-out cross-validation.

some predictions fully concordant with modeled VTAs, while others exhibit only slight overlap.

Interpretation of covariate effects

In the SVM classifier, higher values of beta, HFB (500–2000 Hz), and theta x HFB were positive predictors of therapeutic VTAs, while higher values of theta, alpha, high gamma, HFO, theta x HFB, alpha x beta, beta x HFB, and high gamma x HFO were negative predictors. In general, single covariates were insufficient to accurately forecast effective sites of tissue activation along the DBS trajectory.

Of particular interest was the predictive effect of beta. Plotting beta power against HFB (Fig. 4A) shows that elevated beta is a positive predictor of therapeutic activation sites, but only in the presence of high HFB. Sites with high beta are not activated by therapeutic stimulation when observed with low HFB. HFB-theta interactions show a different effect: low theta power is a positive predictor of therapeutic activation when coincident with high HFB power (Fig. 4B). As HFB is an indicator of STN multiunit activity [49], these interactions indicate that high beta and low theta power are positive predictors of therapeutic activation only within the STN. Overlapping regions of VTA and non-VTA sites show that these covariates must still be interpreted alongside other bands of interest to generate reliable predictions. Alpha-beta and high gamma-HFO interactions were also identified as predictors of therapeutic activation. While the nature of interactions between these oscillations and their relation to VTAs is unclear from visual analysis, the high covariance observed between these pairs of covariates is notable (Fig. 4C–D).

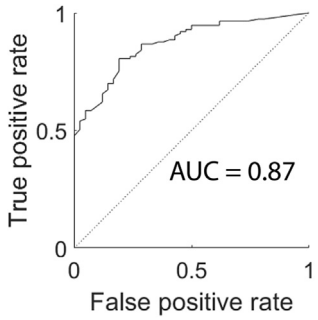

Fig. 3. Receiver operating characteristic curve of smoothed classifier. Calculated from test data. AUC = area under curve.

Discussion

This study yields three notable findings. First, we used atlas-independent, fully individualized patient VTA models to show that clinically effective tissue activation volumes can span a variety of locations, with large proportions of clinically optimized tissue activation observed both above and within the electrophysiologically-defined STN. Second, we mapped high-density, broadband microelectrode recordings to individualized

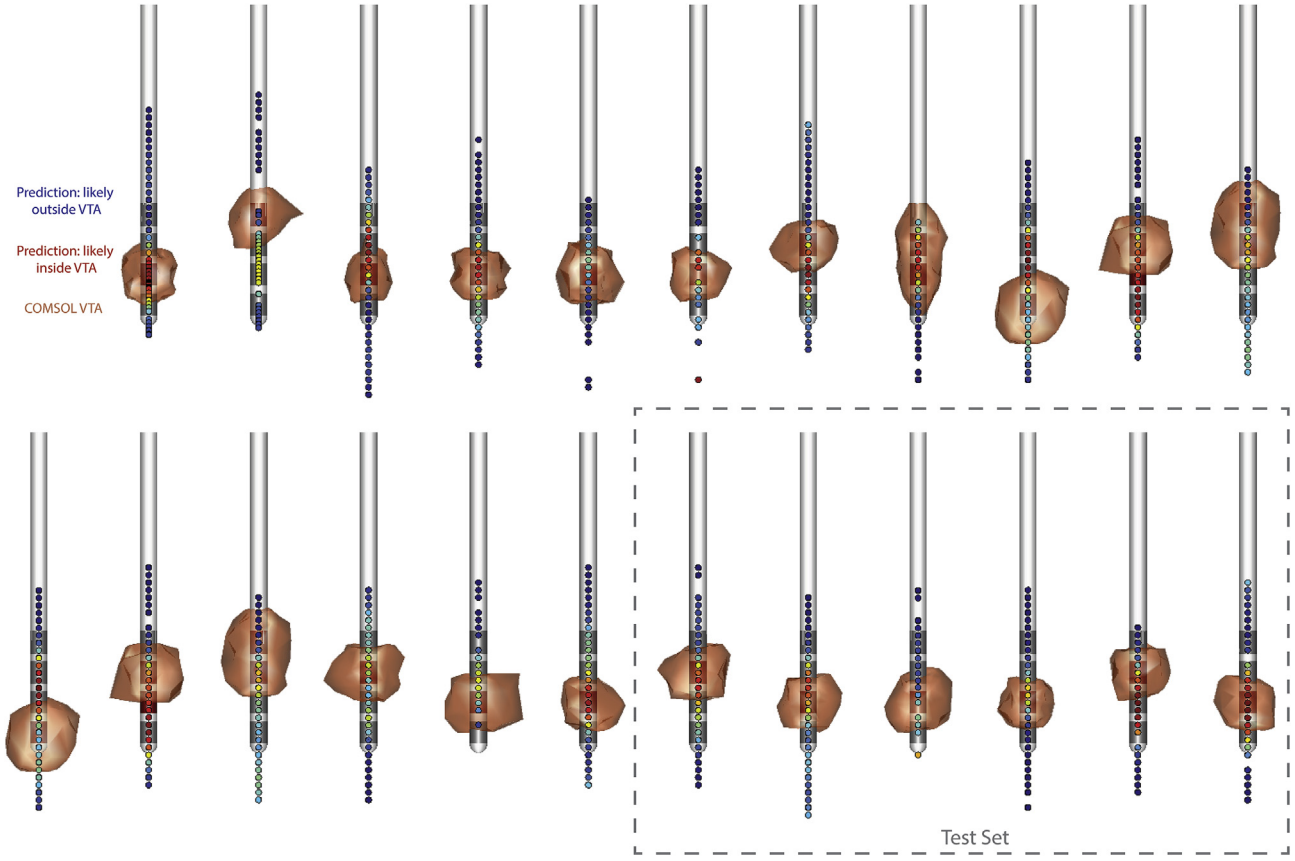

Fig. 2. Therapeutic VTA locations along DBS lead trajectories and smoothed classifier predictions, for all implants. Colors indicate probability of a site being within the therapeutic VTA, with hotter colors indicating higher probability. Active contact is shown in red. Two leads utilized two active contacts (both anodic and synchronized). Test data comprised of six implants is enclosed by the gray dotted line. The implant shown in Fig. 1 is shown as the top left implant in this figure. (For interpretation of the references to color in this figure legend, the reader is referred to the Web version of this article.)

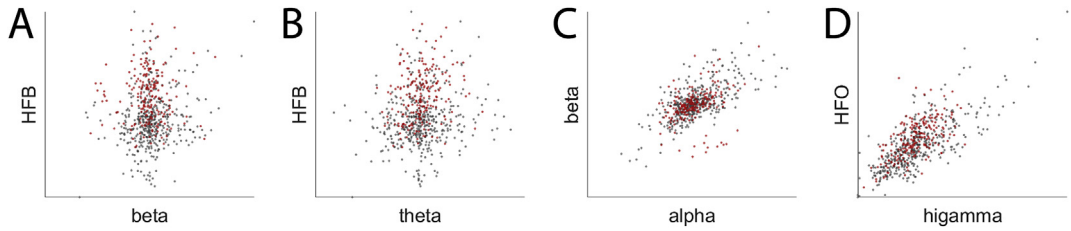

Fig. 4. Main effects of interaction terms plotted against one another show inter-frequency dependence of predictors. Red points indicate sites within modeled VTAs, gray points indicate sites outside. Axes are scaled along arbitrary units. A shows interactions between main effects of the beta x HFB term, B for theta x HFB, C for alpha x beta, and D for high gamma x HFO. (For interpretation of the references to color in this figure legend, the reader is referred to the Web version of this article.)

VTAs, and applied a data-driven method to objectively select and validate ten anatomically agnostic electrophysiological predictors of therapeutic tissue activation in the subthalamic region. Third, we demonstrated and validated a predictive clinical tool to aid DBS lead placement and programming that significantly outperforms a beta-only classifier. When tested on a set of three randomly selected new patients, the algorithm achieved an AUC of 0.87, demonstrating high accuracy and generalizability across patients. In doing so, this study unifies anatomical, electrophysiological, and computational analyses to describe and to validate electrophysiological signatures of regions activated by therapeutic STN DBS.

Logistic LASSO suggested ten electrophysiological predictors of therapeutic VTAs that were subsequently validated by an SVM classifier: theta, alpha, beta, high gamma, HFO, HFB, theta x HFB, alpha x beta, beta x HFB, and high gamma x HFO. While covariates of the relatively simple model used here do not directly reflect physiological mechanisms of treatment or disease pathology, the high predictive value of the SVM does warrant additional attention toward the selected oscillations. Predictive frequency bands identified in this study both support the literature on existing oscillations of interest and suggest new directions of investigation. Power in beta, HFO, alpha, and gamma bands are well-established correlates of Parkinsonian symptoms: beta and HFO are associated primarily with bradykinesia and rigidity, while gamma and alpha oscillations are more often associated with other motor manifestations and affective components of Parkinson disease [26,27,50]. Likewise, subthalamic theta activity has been causally linked to Parkinsonian tremor [51]. Together, these separate frequency bands may independently contribute information about different dimensions of Parkinsonism, each of which can be acted upon by therapeutic DBS. In contrast, HFB power represents STN multiunit activity and therefore provides primarily anatomical information [49]. Evaluation of an HFB-only classifier reveals high predictive value in this anatomical information, as expected from the well-established practice of targeting STN. Other frequency bands likely contribute information to more precisely identify therapeutic activation sites within and adjacent to STN. Notably, spike rate was not selected as a predictive feature of therapeutic VTAs, despite the unique spiking activity of STN. Its exclusion from the LASSO model is likely due to spiking rate's high covariance with HFO and HFB [52,53], which reduces the amount of predictive information it contributes to the model. Elevated spike rate is also often observed in thalamus, which is rarely activated by STN DBS, further reducing its contribution to the predictive model. Note, however, that the microelectrode features used in this study are extracted from only 6 s of recording at each site, which may neglect phenomena that occur at longer time scales and limit the quality of spectral estimation used for other features.

Interaction terms selected by LASSO must be carefully interpreted. The HFB interaction terms identified here provide anatomical context for interpretation of beta and theta power, by restricting their predictive value to sites within STN. Interpretation of the alpha-beta interaction is less obvious. Stein and Bar-Gad [14] suggest that perhaps a single physiologically important oscillation is captured by both alpha and beta bands, in concordance with the high covariance of alpha and beta observed in our data, which the model corrects for using the interaction term. There also exists some evidence that the two bands together are directly linked to presentation of parkinsonian tremor [54]. Similar phenomena may also explain inclusion of the high gamma-HFO interaction in the LASSO model. Perhaps surprisingly, beta-gamma and beta-HFO interactions were excluded. This is likely due to the complex nature of described interactions between beta and high frequency oscillations [31,33], which would not be captured by the simplistic metric used here.

Looking ahead, the prominence of multi-frequency interactions identified and validated here strongly points to avenues of future study. Telkes et al. [32] recently demonstrated that information in beta must be fused with high frequency bands to accurately predict optimal implantation tracks. While the interactions analyzed in this study and by Telkes indicate only that power across frequency bands should be jointly assessed in the predictive model, there also exist more complex measures of interaction that may provide valuable additional information. Sophisticated multi-frequency phenomena, such as phase-amplitude coupling [28,33] and beta burst length [55], have demonstrated physiological relevance. While the regression-based approach described here is unsuitable for analysis of these predictors, the cross-frequency features identified here and in other studies highlight the importance of investigating different components of broadband electrophysiology in concert.

Anatomically, we used atlas-independent, fully individualized VTA models to show that therapeutic effect can be achieved with tissue activation across a variety of sites both within and outside the STN borders. Most therapeutic VTAs activated regions within and above STN, which can be largely achieved with 2.8 V stimulation at dorsal STN. This is in line with prior work pointing to dorsolateral STN as an optimal site of stimulation [3,4]. STN border-based programming was outperformed by microelectrode predictions, although the difference was not statistically significant. However, nuances in performance of the STN border approach necessitate important caveats to this finding. The low positive predictive value (0.45) of STN border-based programming suggests that it activates a large portion of tissue that need not be stimulated for therapeutic effect. Furthermore, the specificity of the approach is likely overestimated. Although key sites of therapeutic activation may be distinct, conventional VTAs must be spatially contiguous, activating neighboring regions. Thus, STN border-based programming and the therapeutic VTAs used for reference exhibit the same systematic error, artifactually inflating the measured specificity. When interpreted together with the anatomical diversity of therapeutic activation regions observed across subjects, as reported by earlier studies [24,56], these findings support opportunities for

additional refinement of DBS targeting and personalized stimulation.

Although this study treats therapeutic tissue activation as a binary variable, presentations of Parkinson disease and its response to STN DBS are known to be multidimensional and varied across patients. A robust body of work suggests that different symptoms may be optimally treated by activation of different subthalamic regions and neural pathways with unique electrophysiological markers [20,26,57,58]. In this view, it is critical to consider the full span of activated tissue when identifying neural markers of DBS targets, as therapy is likely achieved through activation of multiple sites with distinct electrophysiological signatures. Recent work by Telkes et al. [25] showed that different motor subtypes of Parkinson disease present with unique multiband signatures in spatially distinct STN regions. Close examination of results in Fig. 2 reveal large variations in classifier performance between individual implants, suggesting that this phenomenon is likely present in the current study as well. These observations demonstrate the significant potential for further progress in this area. Future work will directly examine these relationships and their utility in treatment optimization.

It is important to note that the analysis here must be understood within the context of some fundamental limitations of the methodology. The spatially contiguous nature of VTAs guarantees that the clinically determined sites of therapeutic activation are biased to include non-therapeutic regions adjacent to clinically important sites of activation. This intrinsic error in our designation of therapeutic activation regions likely introduces significant noise into the algorithm, both in design and validation. Also, the spatial relationship between recorded oscillations and the corresponding synchronous neural population is both imprecise and incompletely understood [59,60], limiting the precision of microelectrode predictions. Spatially smoothing the predictions in this study provided an informative but imperfect remedy for these sources of imprecision.

More generally, it should be noted that tissue activation modeling is complex and makes several specific assumptions. This study utilizes fully individualized anisotropic conductivities and simple activation thresholds to calculate precise patient-specific VTAs. Alternative approaches, such as those employing explicit axon models [61] and driving force calculations [62], may yield different therapeutic activation volumes [63]. At the same time, literature suggests that incorporation of tissue heterogeneity and anisotropy generates reliable activation models [34,35]. Small errors in image co-registration and lead movement after implantation may also introduce errors into our analysis.

Nonetheless, by predicting both the approximate location and span of generalized therapeutic tissue activation volumes, the approach presented here can be used to quickly estimate effective sites and amplitudes of stimulation. Perhaps more importantly, this method significantly restricts the parameter space that must be explored to optimize DBS stimulation parameters. With the introduction of directional DBS leads promising greater therapeutic windows [64–66], new tools such as the one presented here are needed to constrain the greatly expanded parameter space of directional leads to efficiently interrogate potential program settings. Eventually, such targeting methods may be used in concert with parameter optimization algorithms [67–71], potentially achieving even greater STN DBS programming efficiency.

Author contributions section

Charles W. Lu: Conceptualization, Methodology, Software, Validation, Formal Analysis, Investigation, Data Curation, Writing – Original Draft, Writing – Review & Editing, Visualization; **Karlo A. Malaga:** Methodology, Software, Validation, Investigation, Writing – Review & Editing; **Kelvin L. Chou:** Investigation, Resources, Writing – Review & Editing; **Cynthia A. Chestek:** Validation, Writing – Review & Editing, Supervision; **Parag G. Patil:** Validation, Investigation, Resources, Writing – Review & Editing, Supervision, Project Administration, Funding Acquisition.

Funding

This research was supported by the A. Alfred Taubman Medical Institute, the Coulter Foundation, the STIM (Surgical Therapies Improving Movement) Program, and a Ford Foundation Predoctoral Fellowship.

Declaration of competing interest

None.

Acknowledgements

We are grateful for the assistance of Kelly Lupo in image processing and care of patients included in this study.

Appendix A. Supplementary data

Supplementary data to this article can be found online at https://doi.org/10.1016/j.brs.2019.11.013.

References

[1] Hunka K, Suchowersky O, Wood S, Derwent L, Kiss ZH. Nursing time to program and assess deep brain stimulators in movement disorder patients. J Neurosci Nurs 2005;37(4):204–10.
[2] Volkmann J, Moro E, Pahwa R. Basic algorithms for the programming of deep brain stimulation in Parkinson's disease. Mov Disord 2006;21(Suppl 14):S284–9.
[3] Wodarg F, Herzog J, Reese R, Falk D, Pinsker MO, Steigerwald F, et al. Stimulation site within the MRI-defined STN predicts postoperative motor outcome. Mov Disord 2012;27(7):874–9.
[4] Zonenshayn M, Sterio D, Kelly PJ, Rezai AR, Beric A. Location of the active contact within the subthalamic nucleus (STN) in the treatment of idiopathic Parkinson's disease. Surg Neurol 2004;62(3):216–25. discussion 25-6.
[5] Garcia-Garcia D, Guridi J, Toledo JB, Alegre M, Obeso JA, Rodriguez-Oroz MC. Stimulation sites in the subthalamic nucleus and clinical improvement in Parkinson's disease: a new approach for active contact localization. J Neurosurg 2016;125(5):1068–79.
[6] Maks CB, Butson CR, Walter BL, Vitek JL, McIntyre CC. Deep brain stimulation activation volumes and their association with neurophysiological mapping and therapeutic outcomes. J Neurol Neurosurg Psychiatry 2009;80(6):659–66.
[7] Butson CR, Cooper SE, Henderson JM, Wolgamuth B, McIntyre CC. Probabilistic analysis of activation volumes generated during deep brain stimulation. Neuroimage 2011;54(3):2096–104.
[8] Akram H, Sotiropoulos SN, Jbabdi S, Georgiev D, Mahlknecht P, Hyam J, et al. Subthalamic deep brain stimulation sweet spots and hyperdirect cortical connectivity in Parkinson's disease. Neuroimage 2017;158:332–45.
[9] Haynes WI, Haber SN. The organization of prefrontal-subthalamic inputs in primates provides an anatomical substrate for both functional specificity and integration: implications for Basal Ganglia models and deep brain stimulation. J Neurosci 2013;33(11):4804–14.
[10] Gradinaru V, Mogri M, Thompson KR, Henderson JM, Deisseroth K. Optical deconstruction of parkinsonian neural circuitry. Science 2009;324(5925):354–9.
[11] Kumaravelu K, Oza CS, Behrend CE, Grill WM. Model-based deconstruction of cortical evoked potentials generated by subthalamic nucleus deep brain stimulation. J Neurophysiol 2018;120(2):662–80.
[12] McIntyre CC, Mori S, Sherman DL, Thakor NV, Vitek JL. Electric field and stimulating influence generated by deep brain stimulation of the subthalamic nucleus. Clin Neurophysiol 2004;115(3):589–95.
[13] Kuncel AM, Cooper SE, Grill WM. A method to estimate the spatial extent of activation in thalamic deep brain stimulation. Clin Neurophysiol 2008;119(9):2148–58.
[14] Stein E, Bar-Gad I. Beta oscillations in the cortico-basal ganglia loop during parkinsonism. Exp Neurol 2013;245:52–9.
[15] Ince NF, Gupte A, Wichmann T, Ashe J, Henry T, Bebler M, et al. Selection of optimal programming contacts based on local field potential recordings from

subthalamic nucleus in patients with Parkinson's disease. Neurosurgery 2010;67(2):390–7.
[16] Yoshida F, Martinez-Torres I, Pogosyan A, Holl E, Petersen E, Chen CC, et al. Value of subthalamic nucleus local field potentials recordings in predicting stimulation parameters for deep brain stimulation in Parkinson's disease. J Neurol Neurosurg Psychiatry 2010;81(8):885–9.
[17] Zaidel A, Spivak A, Grieb B, Bergman H, Israel Z. Subthalamic span of beta oscillations predicts deep brain stimulation efficacy for patients with Parkinson's disease. Brain 2010;133(Pt 7):2007–21.
[18] Horn A, Neumann WJ, Degen K, Schneider GH, Kuhn AA. Toward an electrophysiological "sweet spot" for deep brain stimulation in the subthalamic nucleus. Hum Brain Mapp 2017;38(7):3377–90.
[19] Guo S, Zhuang P, Hallett M, Zheng Z, Zhang Y, Li J, et al. Subthalamic deep brain stimulation for Parkinson's disease: correlation between locations of oscillatory activity and optimal site of stimulation. Park Relat Disord 2013;19(1):109–14.
[20] Bour LJ, Lourens MA, Verhagen R, de Bie RM, van den Munckhof P, Schuurman PR, et al. Directional recording of subthalamic spectral power densities in Parkinson's disease and the effect of steering deep brain stimulation. Brain Stimul 2015;8(4):730–41.
[21] Tinkhauser G, Pogosyan A, Debove I, Nowacki A, Shah SA, Seidel K, et al. Directional local field potentials: a tool to optimize deep brain stimulation. Mov Disord 2018;33(1):159–64.
[22] Moshel S, Shamir RR, Raz A, de Noriega FR, Eitan R, Bergman H, et al. Subthalamic nucleus long-range synchronization-an independent hallmark of human Parkinson's disease. Front Syst Neurosci 2013;7:79.
[23] Verhagen R, Zwartjes DG, Heida T, Wiegers EC, Contarino MF, de Bie RM, et al. Advanced target identification in STN-DBS with beta power of combined local field potentials and spiking activity. J Neurosci Methods 2015;253:116–25.
[24] Caire F, Ranoux D, Guehl D, Burbaud P, Cuny E. A systematic review of studies on anatomical position of electrode contacts used for chronic subthalamic stimulation in Parkinson's disease. Acta Neurochir 2013;155(9):1647–54. discussion 54.
[25] Telkes I, Viswanathan A, Jimenez-Shahed J, Abosch A, Ozturk M, Gupte A, et al. Local field potentials of subthalamic nucleus contain electrophysiological footprints of motor subtypes of Parkinson's disease. Proc Natl Acad Sci U S A 2018;115(36):E8567–76.
[26] Oswal A, Brown P, Litvak V. Synchronized neural oscillations and the pathophysiology of Parkinson's disease. Curr Opin Neurol 2013;26(6):662–70.
[27] Foffani G, Priori A, Egidi M, Rampini P, Tamma F, Caputo E, et al. 300-Hz subthalamic oscillations in Parkinson's disease. Brain 2003;126(Pt 10):2153–63.
[28] Shreve LA, Velisar A, Malekmohammadi M, Koop MM, Trager M, Quinn EJ, et al. Subthalamic oscillations and phase amplitude coupling are greater in the more affected hemisphere in Parkinson's disease. Clin Neurophysiol 2017;128(1):128–37.
[29] Oswal A, Brown P, Litvak V. Movement related dynamics of subthalmocortical alpha connectivity in Parkinson's disease. Neuroimage 2013;70:132–42.
[30] van Wijk BCM, Pogosyan A, Hariz MI, Akram H, Foltynie T, Limousin P, et al. Localization of beta and high-frequency oscillations within the subthalamic nucleus region. Neuroimage Clin 2017;16:175–83.
[31] Lopez-Azcarate J, Tainta M, Rodriguez-Oroz MC, Valencia M, Gonzalez R, Guridi J, et al. Coupling between beta and high-frequency activity in the human subthalamic nucleus may be a pathophysiological mechanism in Parkinson's disease. J Neurosci 2010;30(19):6667–77.
[32] Telkes I, Jimenez-Shahed J, Viswanathan A, Abosch A, Ince NF. Prediction of STN-DBS electrode implantation track in Parkinson's disease by using local field potentials. Front Neurosci 2016;10:198.
[33] van Wijk BC, Beudel M, Jha A, Oswal A, Foltynie T, Hariz MI, et al. Subthalamic nucleus phase-amplitude coupling correlates with motor impairment in Parkinson's disease. Clin Neurophysiol 2016;127(4):2010–9.
[34] Howell B, McIntyre CC. Analyzing the tradeoff between electrical complexity and accuracy in patient-specific computational models of deep brain stimulation. J Neural Eng 2016;13(3):036023.
[35] Howell B, McIntyre CC. Role of soft-tissue heterogeneity in computational models of deep brain stimulation. Brain Stimul 2017;10(1):46–50.
[36] Patil PG, Conrad EC, Aldridge JW, Chenevert TL, Chou KL. The anatomical and electrophysiological subthalamic nucleus visualized by 3-T magnetic resonance imaging. Neurosurgery 2012;71(6):1089–95. discussion 95.
[37] Houshmand L, Cummings KS, Chou KL, Patil PG. Evaluating indirect subthalamic nucleus targeting with validated 3-tesla magnetic resonance imaging. Stereotact Funct Neurosurg 2014;92(6):337–45.
[38] Tuch DS, Wedeen VJ, Dale AM, George JS, Belliveau JW. Conductivity tensor mapping of the human brain using diffusion tensor MRI. Proc Natl Acad Sci U S A 2001;98(20):11697–701.
[39] Yousif N, Bayford R, Liu X. The influence of reactivity of the electrode-brain interface on the crossing electric current in therapeutic deep brain stimulation. Neuroscience 2008;156(3):597–606.
[40] Kent AR, Grill WM. Analysis of deep brain stimulation electrode characteristics for neural recording. J Neural Eng 2014;11(4):046010.
[41] Logothetis NK, Kayser C, Oeltermann A. In vivo measurement of cortical impedance spectrum in monkeys: implications for signal propagation. Neuron 2007;55(5):809–23.
[42] McNeal DR. Analysis of a model for excitation of myelinated nerve. IEEE Trans Biomed Eng 1976;23(4):329–37.
[43] Rattay F. Analysis of models for external stimulation of axons. IEEE Trans Biomed Eng 1986;33(10):974–7.
[44] Astrom M, Diczfalusy E, Martens H, Wardell K. Relationship between neural activation and electric field distribution during deep brain stimulation. IEEE Trans Biomed Eng 2015;62(2):664–72.
[45] Thompson JA, Lanctin D, Ince NF, Abosch A. Clinical implications of local field potentials for understanding and treating movement disorders. Stereotact Funct Neurosurg 2014;92(4):251–63.
[46] Tibshirani R. Regression shrinkage and selection via the lasso. J R Stat Soc Ser B 1996;58(1):267–88.
[47] Kirkland L, Kanfer F, Millard S. LASSO tuning parameter selection. 2015.
[48] Cortes C, Vapnik V. Support-vector networks. Mach Learn 1995;20(3):273–97.
[49] Novak P, Przybyszewski AW, Barborica A, Ravin P, Margolin L, Pilitsis JG. Localization of the subthalamic nucleus in Parkinson disease using multiunit activity. J Neurol Sci 2011;310(1–2):44–9.
[50] Ozkurt TE, Butz M, Homburger M, Elben S, Vesper J, Wojtecki L, et al. High frequency oscillations in the subthalamic nucleus: a neurophysiological marker of the motor state in Parkinson's disease. Exp Neurol 2011;229(2):324–31.
[51] Tass P, Smirnov D, Karavaev A, Barnikol U, Barnikol T, Adamchic I, et al. The causal relationship between subcortical local field potential oscillations and Parkinsonian resting tremor. J Neural Eng 2010;7(1):16009.
[52] Stark E, Abeles M. Predicting movement from multiunit activity. J Neurosci 2007;27(31):8387–94.
[53] Schlag J, Balvin R. Background activity in the cerebral cortex and reticular formation in relation with the electroencephalogram. Exp Neurol 1963;8(3):203–19.
[54] Hirschmann J, Abbasi O, Storzer L, Butz M, Hartmann CJ, Wojtecki L, et al. Longitudinal recordings reveal transient increase of alpha/low-beta power in the subthalamic nucleus associated with the onset of parkinsonian rest tremor. Front Neurol 2019;10:145.
[55] Tinkhauser G, Pogosyan A, Little S, Beudel M, Herz DM, Tan H, et al. The modulatory effect of adaptive deep brain stimulation on beta bursts in Parkinson's disease. Brain 2017;140(4):1053–67.
[56] Hamel W, Koppen JA, Alesch F, Antonini A, Barcia JA, Bergman H, et al. Targeting of the subthalamic nucleus for deep brain stimulation: a survey among Parkinson disease specialists. World Neurosurg 2017;99:41–6.
[57] Kuhn AA, Volkmann J. Innovations in deep brain stimulation methodology. Mov Disord 2017;32(1):11–9.
[58] Moran A, Bergman H, Israel Z, Bar-Gad I. Subthalamic nucleus functional organization revealed by parkinsonian neuronal oscillations and synchrony. Brain 2008;131(Pt 12):3395–409.
[59] Lempka SF, McIntyre CC. Theoretical analysis of the local field potential in deep brain stimulation applications. PLoS One 2013;8(3):e59839.
[60] Maling N, Lempka SF, Blumenfeld Z, Bronte-Stewart H, McIntyre CC. Biophysical basis of subthalamic local field potentials recorded from deep brain stimulation electrodes. J Neurophysiol 2018;120(4):1932–44.
[61] Gunalan K, Chaturvedi A, Howell B, Duchin Y, Lempka SF, Patriat R, et al. Creating and parameterizing patient-specific deep brain stimulation pathway-activation models using the hyperdirect pathway as an example. PLoS One 2017;12(4):e0176132.
[62] Peterson EJ, Izad O, Tyler DJ. Predicting myelinated axon activation using spatial characteristics of the extracellular field. J Neural Eng 2011;8(4):046030.
[63] Gunalan K, Howell B, McIntyre CC. Quantifying axonal responses in patient-specific models of subthalamic deep brain stimulation. Neuroimage 2018;172:263–77.
[64] Dembek TA, Reker P, Visser-Vandewalle V, Wirths J, Treuer H, Klehr M, et al. Directional DBS increases side-effect thresholds-A prospective, double-blind trial. Mov Disord 2017;32(10):1380–8.
[65] Contarino MF, Bour LJ, Verhagen R, Lourens MA, de Bie RM, van den Munckhof P, et al. Directional steering: a novel approach to deep brain stimulation. Neurology 2014;83(13):1163–9.
[66] Pollo C, Kaelin-Lang A, Oertel MF, Stieglitz L, Taub E, Fuhr P, et al. Directional deep brain stimulation: an intraoperative double-blind pilot study. Brain 2014;137(Pt 7):2015–26.
[67] Pena E, Zhang S, Deyo S, Xiao Y, Johnson MD. Particle swarm optimization for programming deep brain stimulation arrays. J Neural Eng 2017;14(1):016014.
[68] McIntyre CC, Butson CR, Maks CB, Noecker AM. Optimizing deep brain stimulation parameter selection with detailed models of the electrode-tissue interface. Conf Proc IEEE Eng Med Biol Soc 2006;1:893–5.
[69] Teplitzky BA, Zitella LM, Xiao Y, Johnson MD. Model-based comparison of deep brain stimulation array functionality with varying number of radial electrodes and machine learning feature sets. Front Comput Neurosci 2016;10:58.
[70] Xiao Y, Pena E, Johnson MD. Theoretical optimization of stimulation strategies for a directionally segmented deep brain stimulation electrode array. IEEE Trans Biomed Eng 2016;63(2):359–71.
[71] Anderson DN, Osting B, Vorwerk J, Dorval AD, Butson CR. Optimized programming algorithm for cylindrical and directional deep brain stimulation electrodes. J Neural Eng 2018;15(2):026005.